Volume 44 | Number 32 | 28 August 2015 | Pages 14181–14542

Dalton Transactions

An international journal of inorganic chemistry

www.rsc.org/dalton

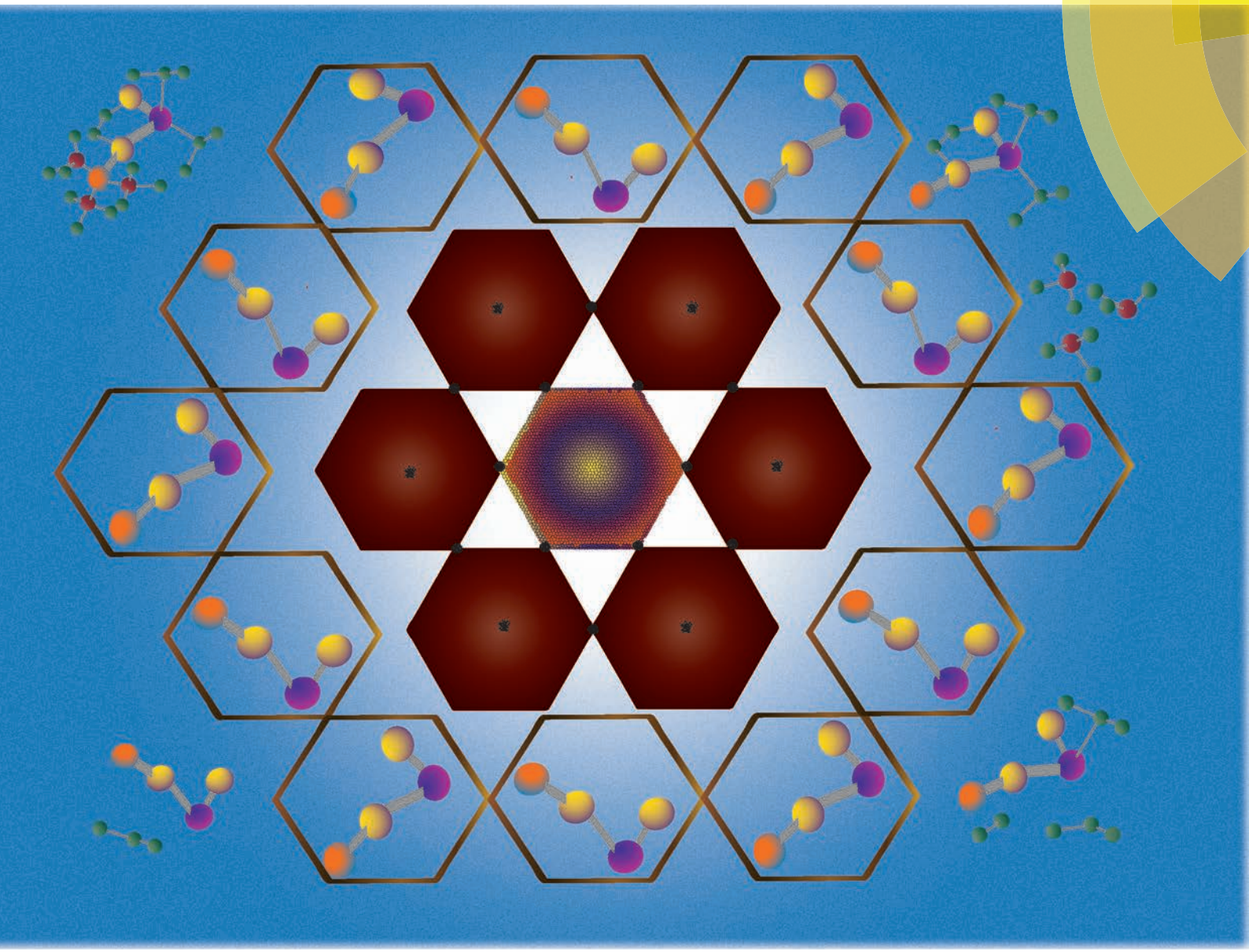

ISSN 1477-9226

ROYAL SOCIETY OF CHEMISTRY

PAPER

Harald Krautscheid *et al.*

Synthesis of $CuInS_2$ nanocrystals from a molecular complex – characterization of the orthorhombic domain structure

Dalton Transactions

PAPER

View Article Online
View Journal | View Issue

Cite this: *Dalton Trans.*, 2015, **44**, 14227

Synthesis of $CuInS_2$ nanocrystals from a molecular complex – characterization of the orthorhombic domain structure†‡

Jorge L. Cholula-Díaz,[a] Gerald Wagner,[b] Dirk Friedrich,[a] Oliver Oeckler[b] and Harald Krautscheid*[a]

Received 29th January 2015,
Accepted 10th May 2015

DOI: 10.1039/c5dt00419e

www.rsc.org/dalton

$CuInS_2$ nanocrystals were synthesized by thermal decomposition of the molecular precursor $[(Me_3P)_3Cu(SC_2H_4S)In^iPr_2]$ in the presence of oleylamine in dioctyl phthalate. According to X-ray diffraction patterns, the as-synthesized $CuInS_2$ nanocrystals crystallize in the wurtzite type structure. High-resolution transmission electron images and selected area electron diffraction patterns reveal a nanodomain structure. The individual domains are approximately 5–10 nm in size and characterized by short-range cation ordering, which assuming hypothetical long-range order, corresponds to an orthorhombic superstructure (space group $Pmc2_1$, a = 4.09 ± 0.01 Å, b = 7.16 ± 0.02 Å and c = 6.56 ± 0.03 Å). The domains are separated by twin and antiphase boundaries.

1 Introduction

The ternary compounds $CuME_2$ (M = Ga, In; E = S, Se) are semiconductors with a direct band gap ranging from 1.0 ($CuInSe_2$) to 2.5 eV ($CuGaS_2$)[1] and high absorption coefficients ($\sim 10^4$ cm^{-1}).[2] Thus, these compounds are very attractive for thin-film based photovoltaic devices.

In 1953, Hahn *et al.*[3] were the first to report the synthesis and crystal structures of 20 ternary compounds with the formula $M^IM^{III}E_2$ (M^I = Cu, Ag; M^{III} = Al, Ga, In, Tl; E = S, Se, Te). All these Harry Hahn phases were found to crystallize in the tetragonal chalcopyrite type (CH) structure, which is an ordered superstructure of the diamond structure of the semiconductors Si and Ge according to the Grimm–Sommerfeld rule.[4] This implies that there must be an average of four electrons per atomic site. The symmetry of the compounds is reduced from the diamond type modification of the main group IV semiconductors (*e.g.* Si, space group $Fd\bar{3}m$)[5] to the binary analogue, the cubic zinc-blende (ZB) type (*e.g.* ZnS, space group $F\bar{4}3m$).[6] In the transition to the ternary compound semiconductors, the symmetry is further reduced to the tetragonal modification (chalcopyrite, space group $I\bar{4}2d$).[3] The tetragonal CH structure is derived from the ZB structure by replacing the Zn^{2+} cations with Cu^+ and group III metal cations in an ordered fashion. This type of ordering approximately doubles the unit cell along [001] of the cubic ZB structure (*e.g.* $CuInS_2$, $a = b$ = 5.52 Å and c = 11.13 Å).[7] In the case of bulk single crystals of $CuInS_2$ and $CuInSe_2$, above a phase transition temperature (T_t), the chalcopyrite structure is converted to the cation disordered cubic ZB modification, as shown in Table 1. According to Schorr *et al.*,[8] this structural phase transition CH → ZB is driven by a Cu-In anti-site occupation.

In analogy to the chalcopyrite structure, orthorhombic variants of $M^IM^{III}E_2$ may be regarded as superstructures of the hexagonal wurtzite type (WZ) modification (*e.g.* WZ-$CuInS_2$ with space group $P6_3mc$, so far only observed in nanocrystals),[9–22] a cation-disordered phase with AB-stacking of identical layers. One orthorhombic structure was identified as the high-temperature phase of bulk single crystal $AgInS_2$ (ht-$AgInS_2$, space group $Pna2_1$),[23] see Table 1. These structures retain the tetrahedral coordination existing in the chalcopyrite and cubic zinc-blende modifications.

In this work the synthesis of nanocrystalline $CuInS_2$ by thermal decomposition of a molecular single-source precursor is reported. The aim of these attempts was to produce "inks", which might be used to deposit ternary light-absorbing $CuInS_2$ thin films by direct liquid coating methods.[45,46] A systematic analysis of selected area electron diffraction (SAED) patterns and high-resolution transmission electron microscopy (HRTEM) images reveals short-range cation order in an average wurtzite type structure.

[a]*Institut für Anorganische Chemie, Universität Leipzig, Johannisallee 29, 04103 Leipzig, Germany. E-mail: krautscheid@rz.uni-leipzig.de; Fax: +49 (0)341-9736199; Tel: +49 (0)341-9736172*
[b]*Institut für Mineralogie, Kristallographie und Materialwissenschaft, Universität Leipzig, Scharnhorststrasse 20, 04275 Leipzig, Germany*

† Dedicated to Professor Manfred Scheer on the occassion of his 60th birthday.

‡ Electronic supplementary information (ESI) available: Details on the synthesis and simultaneous thermal analysis of the molecular complex **1**. Crystallographic data of the hypothetical orthorhombic $CuInS_2$ phases with space groups $Pmn2_1$ and $Pmc2_1$. Temperature-dependent XRD, TEM and HRTEM images, SAED patterns, and EDX data. See DOI: 10.1039/c5dt00419e

Table 1 Modifications and phase transition temperatures of compounds $M^{I}M^{III}E_2$ (M^{I} = Cu, Ag; M^{III} = Ga, In; E = S, Se) in bulk single crystals and nanoparticles. CH: chalcopyrite type, ZB: zinc-blende type, WZ: wurtzite type, O: orthorhombic modification for $AgInS_2$, T_t: transition temperature in bulk single crystals, m.p.: melting point

Compound	Crystal system	Structure type	T_t [°C]	Reference
$CuInS_2$	Tetragonal[a,b]	CH	980 (CH → ZB)	24–26
	Cubic[a,b]	ZB	1045 (ZB → WZ)	10, 24, 27
	Hexagonal[a,b]	WZ	1090 (m.p.)	9–20, 24[c]
	Orthorhombic[b]	—	—	28,[d] 29,[e] (This work)
$CuInSe_2$	Tetragonal[a,b]	CH	806 (CH → ZB)	30–32
	Cubic[a,b]	ZB	986 (m.p.)	30, 33
	Hexagonal[b]	WZ	—	34
	Orthorhombic[a]	TlI	—	35[f]
	Cubic[a]	NaCl	—	35[g]
$CuGaS_2$	Tetragonal[a,b]	CH	1240 (m.p.)	3, 36, 37
	Hexagonal[b]	WZ	—	37–40
	Cubic[b]	NaCl	—	39[h]
$AgInS_2$	Tetragonal[a,b]	CH	620 (CH → O)	23, 41, 42
	Orthorhombic[a,b]	β-$NaFeO_2$	880 (m.p.)	41, 43
	Cubic[b]	ZB	—	44

[a] Modification observed in bulk single crystals. [b] Modification observed in nanocrystalline materials. [c] Binsma *et al.* assumed this high-temperature modification to be WZ. [d] Space group $Pmc2_1$. [e] A range of cation-ordered wurtzite-like structures. [f] Modification observed at a pressure of 53 GPa (space group *Cmcm*). [g] Modification observed at a pressure of 7.6 GPa. [h] Modification observed at a pressure above 15.9 GPa.

2 Results and discussion

2.1 Synthesis

The molecular precursor complex $[(Me_3P)_3Cu(SC_2H_4S)In^iPr_2]$ (**1**), consisting of a tris(trimethylphosphino)-copper(I) unit coordinated to a sulfur atom of a $^iPr_2In(S_2C_2H_4)$ group with a chelating 1,2-ethanedithiolate ligand, as shown in Fig. 1, was mixed with oleylamine (OLA) in dioctyl phthalate (DOP). During the heating process, changes in the color of the suspension/solution were observed. These changes may be related to the formation of different intermediates. Firstly, at ~200 °C a green-yellow suspension may correspond to the formation of a $[Cu(SC_2H_4S)In^iPr_2]$ complex formed after the loss of PMe_3 molecules. This assumption is supported by simultaneous thermal analysis (STA) of the molecular complex **1** under helium atmosphere (see Fig. S1 and S2 in ESI‡). At higher temperatures (~270 °C) a brownish colored suspension may indicate further decomposition. Finally, at ~300 °C a black/brown suspension points out the synthesis of $CuInS_2$ nanocrystals.

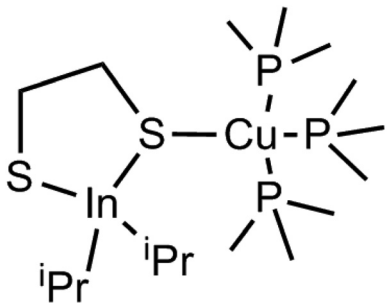

Fig. 1 Molecular structure of $[(Me_3P)_3Cu(SC_2H_4S)In^iPr_2]$ (**1**).

A capping agent (OLA) was added to the reaction mixture in order to make the semiconductor particles dispersible in non polar organic solvents and to obtain monodisperse nanoparticles.[47–50] Although different amounts of capping agent were employed, the reaction product always consists of aggregated nanoparticles (NP-CIS). In a similar strategy, Castro *et al.*[51] synthesized nanocrystals of $CuInS_2$ using the molecular precursor $[(PPh_3)_2CuIn(SEt)_4]$ and DOP as solvent. They observed that aggregated nanoparticles are formed in absence of a proper coordinating ligand.

2.2 X-ray diffraction

The X-ray powder diffraction (XRD) pattern of the as-synthesized NP-CIS sample is shown in Fig. 2 together with the calculated patterns for chalcopyrite (CH) and wurtzite type (WZ), and for the hypothetical orthorhombic $Pmc2_1$ modification of $CuInS_2$ (see ESI, Table S3‡ for crystallographic data). All observed reflections correspond to WZ-$CuInS_2$ and side phases were not detected. The hexagonal lattice parameters were calculated to be a = 3.916(2) Å and c = 6.434(3) Å, which are in good agreement with reported values (a = 3.9065 Å and c = 6.4289 Å).[9,15] The experimental intensity ratios of the 100, 002 and 101 reflections, expressed as $I_{100} : I_{002} : I_{101}$, are 1.3 : 1.0 : 1.5. These ratios are in approximate agreement with the expected values (1.4 : 1.0 : 1.9).[9] It is noticed that the intensity of the 002 reflection is slightly higher than that reported by Qi *et al.*,[9] indicating that there is a small content of the tetragonal modification in the NP-CIS sample, since the reflection 112 for chalcopyrite type $CuInS_2$ appears almost at the same diffraction angle.

The temperature-dependent XRD pattern shows a phase transformation from the metastable cation-disordered hexagonal structure (wurtzite type) to the thermodynamically stable

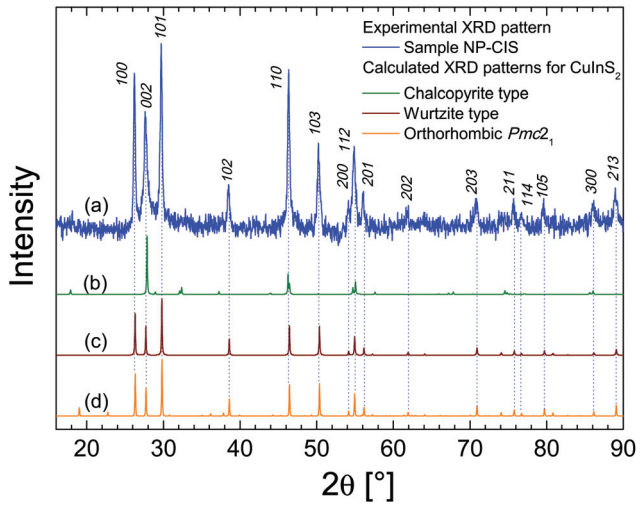

Fig. 2 Comparison of (a) the experimental XRD pattern of the as-synthesized NP-CIS sample measured at room temperature and the calculated XRD patterns for $CuInS_2$: (b) chalcopyrite type $I\bar{4}2d$,[7] (c) wurtzite type $P6_3mc$,[9] and (d) hypothetical orthorhombic $Pmc2_1$ modification. Miller indices for wurtzite type $CuInS_2$.

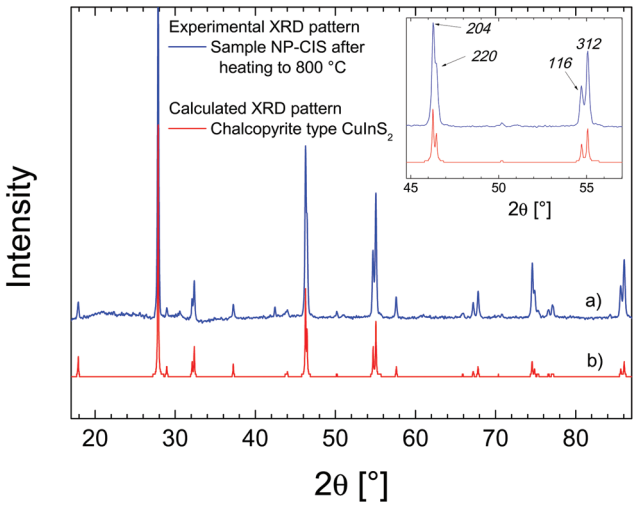

Fig. 3 (a) XRD pattern of the NP-CIS sample recorded at room temperature after been heated to a maximum temperature of 800 °C. (b) Calculated XRD pattern of chalcopyrite type $CuInS_2$.[7] Inset: detail showing the splitting of the 204/220 and 116/312 reflections of the experimental XRD pattern presented in (a).

tetragonal structure (chalcopyrite type), see Fig. S4.‡ By increasing the temperature at a heating rate of ≈4 K min^{-1}, the 002 reflection of the hexagonal structure at 2θ = 27.8° transforms into the corresponding 112 reflection of tetragonal $CuInS_2$ at 2θ = 27.9°. At approximately 550 °C, the 100 and 101 reflections at 2θ = 26.3° and 29.8°, respectively, disappear completely. Similar results have been reported for thermally treated WZ-$CuInS_2$ samples by Qi *et al.*[9] They observed a complete phase transformation in the temperature range of 500–600 °C. Moreover, the XRD pattern of our NP-CIS sample, recorded at room temperature after heating to a maximum temperature of 800 °C, shows that the splitting of the 220/204 and 116/312 reflections of the tetragonal structure is well resolved, as shown in Fig. 3. Minor amounts of In_2O_3 [52] and a copper–indium alloy $Cu_{11}In_9$ [53] are similar to those found in the residue of **1** after been heated up to 900 °C (Fig. S3‡) and to those reported by Friedrich *et al.*[54] in thermolysis studies of the molecular complex $[(^iPr_3PCu)_2(In^iPr_2)_2(SC_2H_4S)_2]$.

2.3 Elemental composition and morphology

The spatial distributions of Cu, In and S (determined by energy-dispersive X-ray spectroscopy (EDX) mapping) are relatively homogeneous in the NP-CIS sample, as seen in Fig. S5.‡ This is an indication that our sample is composed of monophasic $CuInS_2$ nanocrystals, rather than nanocomposites of copper and indium sulfides.[55,56]

According to EDX analyses (Fig. S6‡) for three nanocrystals 1, 2 and 3 shown in Fig. 4, the average elemental composition for the three crystals is 25.2 ± 0.5 at% Cu, 21.2 ± 0.9 at% In and 53.6 ± 0.5 at% S (Table 2), which slightly differs from the formula $CuInS_2$. The wurtzite phase allows flexibility of the elemental composition, due to copper and indium sharing

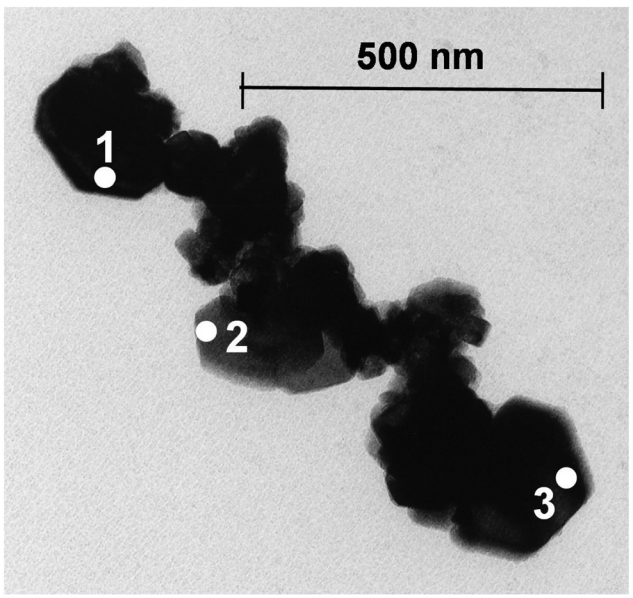

Fig. 4 TEM image of hexagonal nanocrystals in the NP-CIS sample.

Table 2 Elemental composition of the three nanocrystals labeled in Fig. 4

Element	Crystal 1	Crystal 2	Crystal 3	Average
at% Cu	25.3	25.8	24.5	25.2 ± 0.5
at% In	21.6	19.9	22.1	21.2 ± 0.9
at% S	53.1	54.3	53.4	53.6 ± 0.5

one common lattice site.[12,24,57] Transmission electron microscopy (TEM) images revealed that the NP-CIS sample consists of hexagonal nanoplates with edge lengths and thicknesses in the size ranges of 90–180 nm and 30–60 nm, respectively, as seen in Fig. 4 and S7.‡

2.4 HRTEM images and SAED patterns

Plate-like crystallites with hexagonal shape (Fig. S7‡) were selected for HRTEM investigations, Fig. 5 shows a representative HRTEM image. A series of SAED patterns seems to contain reflections in addition to the reflections that correspond to the wurtzite structure type. Particularly, diffraction patterns taken along beam direction (bd) $[001]_h$ (the index h indicates that the direction refers to the hexagonal basis of the wurtzite type) show diffuse lines (streaks) that form a Kagomé net, see inset of Fig. 5. Upon tilting the crystal in the electron beam by just a few degrees (~5°), the Kagomé pattern disappears; this indicates that the lines are indeed streaks and not sections through diffuse planes. Consequently, the additional intensities observed in other SAED patterns are not "superstructure reflections", but they correspond to sections through these lines.

HRTEM images with electron beam parallel $[001]_h$, see Fig. 5, show contrast features that do not agree with wurtzite type $CuInS_2$ (an exception is the encircled area that does not show significant contrast variation, either due to incomplete ordering or to the superposition of different domains along the beam direction). Instead, they indicate an orthorhombic superstructure, obviously caused by cation ordering. Possible structure models can be derived by group-subgroup relationships.[58] Starting from $P6_3mc$ (4 atoms per unit cell, lattice parameters from literature: a_h = 3.9065 Å, c_h = 6.4289 Å),[9] the *translationengleiche* $t2$ subgroup $Cmc2_1$ (8 atoms per unit cell, $a \approx 3.907$ Å, $b \approx 6.767$ Å, $c \approx 6.429$ Å) cannot explain additional reflections of a superstructure and enables no cation ordering. *klassengleiche* $k2$ transformations lead to four possible maximal subgroups: $Pbn2_1$ (= $Pna2_1$), $Pmn2_1$, $Pbc2_1$ (= $Pca2_1$) and $Pmc2_1$. These cells contain 8 atoms and are not C centered, the lattice parameters remain unchanged. The $Pbn2_1$ and $Pbc2_1$ structures exhibit only one cation position and thus do not enable Cu/In cation ordering. In contrast, cation ordering is possible in $Pmn2_1$ and $Pmc2_1$. Both structures are depicted in Fig. 6. The ordered orthorhombic structure of ht-$AgInS_2$ exhibits the space group $Pna2_1$,[23] which is a *klassengleiche* subgroup of $Pbc2_1$ (= $Pca2_1$). This would mean an additional superstructure (16 atoms per unit cell) and additional reflections, which in our case are not observed experimentally. Also, there is no diffuse intensity at the corresponding lattice nodes.

In order to distinguish between the relevant models in $Pmn2_1$ and $Pmc2_1$, the experimental SAED patterns of 24 different zone axes for 14 individual $CuInS_2$ nanocrystals were compared with the calculated ones. The resulting averaged cell dimensions are a_o = 4.09 ± 0.01 Å, b_o = 7.16 ± 0.02 Å and c_o =

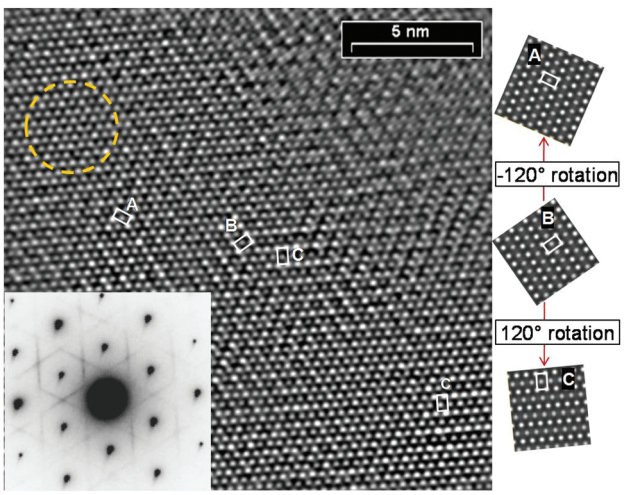

Fig. 5 Experimental HRTEM image of a $CuInS_2$ nanocrystal (zone axis $[001]_h$, Fourier filtered using the maxima at the wurtzite type's lattice nodes, 000 not included) and SAED pattern of the whole nanocrystal with all its domains (inset); the simulated HRTEM images (see the caption of Fig. 8 for the details concerning the simulations) on the right represent the three possible orientations of orthorhombic domains for $Pmc2_1$ (±120° rotation about the axis perpendicular to the plane of the page); the encircled area corresponds to the $P6_3mc$ wurtzite type (see text for explanation).

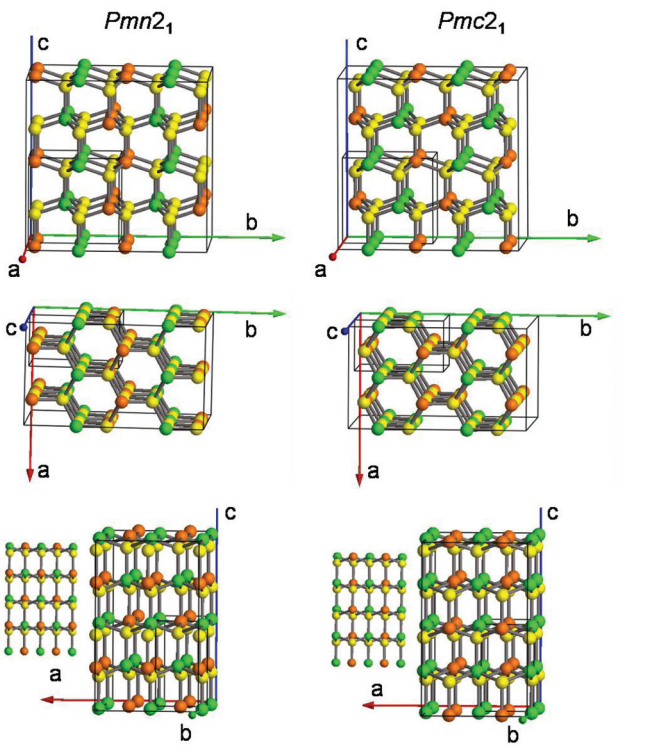

Fig. 6 Hypothetical ordered wurtzite-like crystal structures for $CuInS_2$ with space groups $Pmn2_1$ and $Pmc2_1$; In green, Cu orange, S yellow; perspective views approximately along $[100]_o$ (top), $[001]_o$ (middle) and $[010]_o$ (bottom) reveal the differences in cation ordering between the two models.

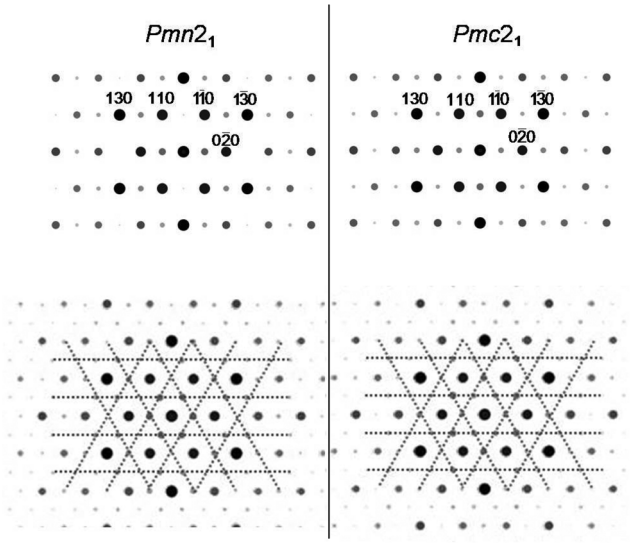

Fig. 7 Simulated electron diffraction patterns for single orthorhombic crystals (top) and for threefold pseudo-hexagonal twins (bottom) for ordered superstructures of wurtzite type $CuInS_2$ assuming the space groups $Pmn2_1$ (left) and $Pmc2_1$ (right): only for $Pmc2_1$ the superstructure reflections of weaker intensity (gray) occupy all intersection points of the Kagomé net (indicated in gray lines).

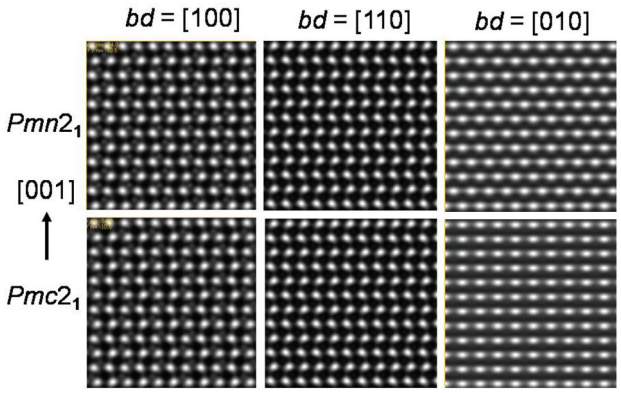

Fig. 8 Simulated HRTEM images of $CuInS_2$ for $Pmn2_1$ and $Pmc2_1$ for zone axes $[100]_o$, $[110]_o$ and $[010]_o$ (parameters for calculation: accelerating voltage U = 200 kV, aperture 20 nm^{-1}, electron energy spread 1.5 eV, semi-convergence 1 mrad, C_S = 1.2 mm, C_C = 1.2 mm, crystal thickness 11 nm, Δf = −54 nm for $[100]_o$ and $[110]_o$ and −88 nm for $[010]_o$).

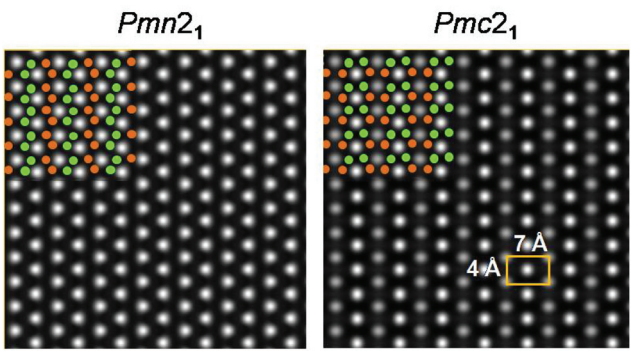

Fig. 9 Simulated HRTEM images of $CuInS_2$ for $Pmn2_1$ and $Pmc2_1$ for the zone axis $[001]_o$ (parameters for calculation see the caption of Fig. 8, Δf = −54 nm); the insets indicate the cation positions (Cu orange and In green); the orthorhombic cell with $a \approx 4$ Å and $b \approx 7$ Å cell is marked by a rectangle.

6.56 ± 0.03 Å (the index o is for the orthorhombic system). Assuming the structure model in $Pmc2_1$, a SAED pattern as shown in Fig. 7 (top right) would be observed, which does not resemble the Kagomé net in the inset of Fig. 5. However, threefold twinning as shown in Fig. 7 (bottom right) results in a pattern, where the superstructure reflections occupy the intersection points of the Kagomé-net-like diffuse lines. If the structure model in $Pmn2_1$ is assumed (Fig. 7, left), due to the extremely weak intensity of 100 (only present for double diffraction) and missing 030, not all intersection positions would be occupied by diffraction spots. From this qualitative view, $Pmc2_1$ seems more reasonable and is confirmed by HRTEM (*vide infra*).

The diffuse streaks observed in the experimental SAED pattern in the inset of Fig. 5 correspond to a three-fold twinned arrangement of nanodimensional domains with layer-like cation order, resembling to the situation in $Na_{22}Ba_{14}CaN_6$.[59] Due to the small size of the super-structured domains, there are no sharp superstructure reflections; however, diffuse streaks connect the hypothetical superstructure reflections (gray lines in Fig. 7, bottom right), resembling domain-wall scattering. However, sometimes weak but distinct maxima are suggested at the intersection points of the Kagomé net and indicate larger ordered domains.

HRTEM images enable a much more unequivocal interpretation. Whereas simulated images for the models in $Pmn2_1$ and $Pmc2_1$ along the zone axes $[100]_o$ and $[110]_o$ (corresponding to the orthorhombic setting) do not differ significantly under same imaging conditions (see Fig. 8), simulated images along $[010]_o$ and $[001]_o$, which corresponds to $[001]_h$, are very different as demonstrated in Fig. 8 and 9, respectively. For $Pmn2_1$ and along $[001]_o$, the contrast is uniformly bright, whereas for $Pmc2_1$ the cation ordering scheme leads to gray and much brighter contrasts for the "channels" of the structure (Fig. 9). Due to the cation arrangement in $Pmn2_1$ (Fig. 6), the simulated images with beam direction bd = $[010]_o$ vary for $Pmn2_1$ and $Pmc2_1$, as shown in Fig. 8, and in more detail, in Fig. S8.‡ Experimental HRTEM images fit well with the simulated images for $Pmc2_1$, as seen in Fig. 5 and 10.

Experimental HRTEM images along $[110]_o$ and $[010]_o$ (Fig. 10) correspond well to the calculated ones. In the pattern with bd = $[010]_o$ the $10l$ reflections characteristic for orthorhombic ordered superstructure are weak, but present. In the pattern with bd = $[110]_o$ the forbidden 001 is caused by double diffraction. They further prove that there is no change of the hexagonal ...ABABAB... stacking sequence towards a chalcopyrite type arrangement with a "cubic" ...ABCABCA... stacking, which was observed in a $CuGaS_2$ nanoplate by Kluge *et al.*[38]

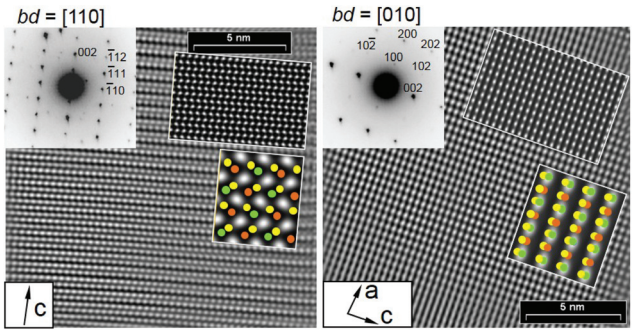

Fig. 10 Experimental HRTEM images (zone axes $[110]_o$ and $[010]_o$, Fourier filtered using the maxima at the wurtzite type's lattice nodes, 000 not included) and SAED patterns (top left insets) of $CuInS_2$ nanocrystals; further insets show simulated images for $Pmc2_1$ (parameters for calculation as in Fig. 8, Δf = −88 nm); the enlarged insets illustrate the atom positions (Cu orange, In green and S yellow).

The well-pronounced contrast pattern in Fig. 5 (HRTEM image along $[001]_h$) clearly shows that this crystallite consists of several nanodimensional twin domains. These correspond to the hexagonal → orthorhombic transition which involves threefold twinning, *i.e.* the individual domains are rotated by 120° around their common [001] direction (same index for hexagonal and orthorhombic setting). It is very likely that this relationship corresponds to an actual phase transition and not to twinning due to crystal growth. Under the chosen conditions for the thermolysis of the molecular complex $[(Me_3P)_3Cu(SC_2H_4S)In^iPr_2]$ (**1**), *i.e.* in DOP as a solvent and in the presence of an amine (OLA) as a stabilizing ligand, probably the randomly disordered truly hexagonal wurtzite type (WZ) structure was formed as a metastable phase. According to Chang and Waclawik,[20] and Gong *et al.*,[27] the synthesis of WZ-$CuInS_2$ nanocrystals is preceded by the formation of a relative stable $CuIn(SR)_x$ complex as intermediate. In our work, this type of intermediate is already present in the molecular complex **1**, see Fig. 1; it is expected that the presence of OLA in the reaction mixture makes the intermediate complex ($[Cu(SC_2H_4S)In^iPr_2]$) comparatively more stable than the exclusively use of DOP. Thus, on one hand the nucleation rate may have been slow, but on the other hand the growth rate was fast; these conditions promoted the formation of metastable WZ-$CuInS_2$ nanoplates as the final thermolysis product, which is in good agreement with the observations in the literature.[20,27] Nevertheless, as the cations exhibit a pronounced tendency towards an ordered structure (thermodynamically more stable),[60] cooling leads to the simplest possible ordered arrangement, *i.e.* orthorhombic domains whose structure would exhibit the space group $Pmc2_1$ in extended crystals. As the superstructure formation is diffusion-controlled, only short-range cation ordering occurs. Therefore, only small domains of the $CuInS_2$ nanocrystals exhibit the structure corresponding to the space group $Pmc2_1$. This leads to the observed well-aligned diffuse intensities forming a Kagomé net in the [001] electron diffraction pattern. Since the ordering involves a *klassengleiche* transition from $Cmc2_1$ to the maximal subgroup $Pmc2_1$, a phase transition is expected to cause antiphase boundaries, which can be clearly seen in Fig. S9.‡ Recently Shen *et al.*[29] interpreted the electron diffraction pattern of $CuInS_2$ nanoplates as a range of cation-ordered wurtzite-like structures. The unit cell parameters, predicted by DFT calculations, for one of their proposed structures (a = 3.95 Å, b = 6.82 Å, c = 6.49 Å)[29] correspond to those determined by experimental SAED patterns in this work. Furthermore, the atomic coordinates in orthorhombic $CuInS_2$ are consistent with the positions in space group $Pmc2_1$ (see ESI, Table S3‡).

3 Experimental section

3.1 Synthesis of nanocrystalline $CuInS_2$

The organometallic compound $[(Me_3P)_3Cu(SC_2H_4S)In^iPr_2]$ (**1**)[61] (see ESI‡ for details on its synthesis) was used as single-source precursor for the synthesis of nanocrystalline $CuInS_2$. Oleylamine (OLA, technical grade) and dioctyl phthalate (DOP, ≥95.5%) were purchased from Sigma-Aldrich and saturated with N_2 at 100 °C under constant N_2 flow prior to use.

The preparation of the precursor solution, as well as the synthesis of the $CuInS_2$ nanocrystals were performed using standard Schlenk techniques for air and moisture-sensitive compounds. 200 mg (≈0.3 mmol) of the molecular precursor **1** were suspended in 7 mL DOP at room temperature. 530 μL OLA were added to the reaction mixture as capping agent. The temperature was initially raised to 200 °C for 10 min in order to increase the solubility of the molecular precursor in DOP (it was observed that a green-yellow suspension was formed). Finally, the suspension was heated to constant reflux for 60 min, in the meanwhile, the suspension turned to a brownish color at ~270 °C. The resulting suspension (a black/brown powder can be observed on the walls of the Schlenk flask) was allowed to cool down to room temperature and 15 mL of toluene were added to decrease the viscosity of the reaction mixture. From this point, the product can be handled in air without evident decomposition. The powder suspended in the liquid mixture was isolated by centrifugation for 20 min at 4000 rpm. The brownish supernatant was discarded and the powder was washed by redispersing it in acetone and separated again by centrifugation. The washing process was repeated until the supernatant was colorless. The final product was dried under reduced pressure at room temperature. It consists of a black powder and can relatively easily be suspended in acetone or toluene, but the suspensions are not stable for more than *ca.* 10 min.

3.2 Characterization techniques

XRD patterns were measured on a STOE Stadi P diffractometer in a modified Debye–Scherrer mode with Cu Kα1 radiation (λ = 1.540598 Å). Room temperature data were recorded with a linear PSD; high temperature measurements were performed with a STOE furnace type 0.65.3 and a curved image plate detector.

TEM was performed using a Philips CM 200 STEM equipped with a double-tilt specimen holder and a LaB_6 cathode with an accelerating voltage of $U = 200$ kV. A calibrated EDX system (EDAX) is integrated to the TEM for qualitative and quantitative elemental analysis. Simulations of SAED patterns and HRTEM images were done by the JEMS software package.[62] Nanocrystalline $CuInS_2$ samples for TEM and EDX measurements were prepared by dispersing the as-synthesized $CuInS_2$ powder in ethanol by ultrasonic treatment followed by drop casting onto carbon-coated molybdenum TEM grids. For HRTEM images and SAED patterns, the samples were prepared by a method described in the ESI.‡

4 Conclusions

We have presented the synthesis of $CuInS_2$ nanocrystals *via* a solution-based route using a molecular complex as single-source precursor. According to its XRD pattern, the thermolysis product crystallized in the metastable hexagonal wurtzite $CuInS_2$ phase, since superstructure reflections are extremely weak and broad. A series of experimental SAED patterns does not exactly match with those calculated for a wurtzite structure. Moreover, SAED patterns and HRTEM images along beam direction [001] clearly show twin nanodomains and antiphase boundaries. Thus, the TEM investigation strongly indicates that initially a wurtzite type structure with random cation disorder is formed that upon cooling undergoes a phase transition towards an orthorhombic structure with space group $Pmc2_1$. Finally, this study may open up the possibility to investigate the physical and chemical properties of a new type structure in the nanocrystalline $CuInS_2$ material.

Acknowledgements

J.L. Cholula-Díaz thanks Graduate School of Natural Sciences "BuildMoNa" of Universität Leipzig for a fellowship. Financial support by Universität Leipzig and PbF-1 is gratefully acknowledged. This work was funded by the European Union (ESF) and the Free State of Saxony.

References

1 M. Grundmann, *The Physics of Semiconductors: An Introduction Including Devices and Nanophysics*, Springer-Verlag, Berlin, Heidelberg, 2006, p. 12.
2 H.-W. Schock, *Thin-Film Solar Cells: Next Generation Photovoltaics and Its Applications*, Springer-Verlag, 2004, p. 165.
3 H. Hahn, G. Frank, W. Klingler, A. D. Meyer and G. Stoerger, *Z. Anorg. Allg. Chem.*, 1953, **271**, 153–170.
4 H. G. Grimm and A. Sommerfeld, *Z. Phys.*, 1926, **36**, 36–59.
5 B. N. Dutta, *Phys. Status Solidi B*, 1962, **2**, 984–987.
6 C. Yeh, Z. W. Lu, S. Froyen and A. Zunger, *Phys. Rev. B*, 1992, **46**, 10086–10097.
7 S. C. Abrahams and J. L. Bernstein, *J. Chem. Phys.*, 1973, **59**, 5415–5422.
8 S. Schorr, G. Geandier and B. V. Korzun, *Phys. Status Solidi C*, 2006, **3**, 2610–2613.
9 Y. Qi, Q. Li, K. Tang, Z. Liang, Z. Ren and X. Liu, *J. Phys. Chem. C*, 2009, **113**, 3939–3944.
10 D. Pan, L. An, Z. Sun, W. Hou, Y. Yang, Z. Yang and Y. Lu, *J. Am. Chem. Soc.*, 2008, **130**, 5620–5621.
11 K. Nose, Y. Soma, T. Omata and S. Otsuka-Yao-Matsuo, *Chem. Mater.*, 2009, **21**, 2607–2613.
12 M. E. Norako, M. A. Franzman and R. L. Brutchey, *Chem. Mater.*, 2009, **21**, 4299–4304.
13 B. Koo, R. N. Patel and B. A. Korgel, *Chem. Mater.*, 2009, **21**, 1962–1966.
14 S. K. Batabyal, L. Tian, N. Venkatram, W. Ji and J. J. Vittal, *J. Phys. Chem. C*, 2009, **113**, 15037–15042.
15 M. Kruszynska, H. Borchert, J. Parisi and J. Kolny-Olesiak, *J. Am. Chem. Soc.*, 2010, **132**, 15976–15986.
16 P. Bera and S. I. Seok, *J. Solid State Chem.*, 2010, **183**, 1872–1877.
17 X. Sheng, L. Wang, Y. Luo and D. Yang, *Nanoscale Res. Lett.*, 2011, **6**, 562.
18 X. Lu, Z. Zhuang, Q. Peng and Y. Li, *CrystEngComm*, 2011, **13**, 4039–4045.
19 W.-C. Huang, C.-H. Tseng, S.-H. Chang, H.-Y. Tuan, C.-C. Chiang, L.-M. Lyu and M. H. Huang, *Langmuir*, 2012, **28**, 8496–8501.
20 J. Chang and E. R. Waclawik, *CrystEngComm*, 2013, **15**, 5612–5619.
21 D. Aldakov, A. Lefrançois and P. Reiss, *J. Mater. Chem. C*, 2013, **1**, 3756–3776.
22 J. Kolny-Olesiak and H. Weller, *ACS Appl. Mater. Interfaces*, 2013, **5**, 12221–12237.
23 A. A. Vaipolin, Y. V. Rud' and I. V. Rozhdestvenskaya, *Cryst. Res. Technol.*, 1988, **23**, 337–341.
24 J. J. M. Binsma, L. J. Giling and J. Bloem, *J. Cryst. Growth*, 1980, **50**, 429–436.
25 S. L. Castro, S. G. Bailey, R. P. Raffaelle, K. K. Banger and A. F. Hepp, *J. Phys. Chem. B*, 2004, **108**, 12429–12435.
26 C. Sun, Z. Cevher, J. Zhang, B. Gao, K. Shum and Y. Ren, *J. Mater. Chem. A*, 2014, **2**, 10629–10633.
27 F. Gong, S. Tian, B. Liu, D. Xiong and X. Zhao, *RSC Adv.*, 2014, **4**, 36875–36881.
28 V. M. Dzhagan, A. P. Litvinchuk, M. Y. Valakh, M. Kruszynska, J. Kolny-Olesiak, C. Himcinschi and D. R. T. Zahn, *Phys. Status Solidi A*, 2014, **211**, 195–199.
29 X. Shen, E. A. Hernández-Pagan, W. Zhou, Y. S. Puzyrev, J.-C. Idrobo, J. E. Macdonald, S. J. Pennycook and S. T. Pantelides, *Nat. Commun.*, 2014, **5**, 5431.
30 J. Parkes, R. D. Tomlinson and M. J. Hampshire, *J. Cryst. Growth*, 1973, **20**, 315–318.
31 S. Schorr and G. Geandier, *Cryst. Res. Technol.*, 2006, **41**, 450–457.
32 Z. Han, D. Zhang, D. Zhang, R. Hong, Q. Chen, C. Tao, Y. Huang, Z. Ni and S. Zhuang, *Superlattices Microstruct.*, 2013, **62**, 156–165.

33 S. Li, Z. Zhao, Q. Liu, L. Huang, G. Wang, D. Pan, H. Zhang and X. He, *Inorg. Chem.*, 2011, **50**, 11958–11964.
34 M. E. Norako and R. L. Brutchey, *Chem. Mater.*, 2010, **22**, 1613–1615.
35 T. Bovornratanaraks, V. Saengsuwan, K. Yoodee, M. I. McMahon, C. Hejny and D. Ruffolo, *J. Phys.: Condens. Matter*, 2010, **22**, 355801.
36 M. Kokta, J. R. Carruthers, M. Grasso, H. M. Kasper and B. Tell, *J. Electron. Mater.*, 1976, **5**, 69–89.
37 S.-H. Chang, B.-C. Chiu, T.-L. Gao, S.-L. Jheng and H.-Y. Tuan, *CrystEngComm*, 2014, **16**, 3323–3330.
38 O. Kluge, D. Friedrich, G. Wagner and H. Krautscheid, *Dalton Trans.*, 2012, **41**, 8635–8642.
39 N. Xiao, L. Zhu, K. Wang, Q. Dai, Y. Wang, S. Li, Y. Sui, Y. Ma, J. Liu, B. Liu, G. Zou and B. Zou, *Nanoscale*, 2012, **4**, 7443–7447.
40 Y.-H. A. Wang, X. Zhang, N. Bao, B. Lin and A. Gupta, *J. Am. Chem. Soc.*, 2011, **133**, 11072–11075.
41 R. S. Roth, H. S. Parker and W. S. Brower, *Mater. Res. Bull.*, 1973, **8**, 333–338.
42 T. Torimoto, M. Tada, M. Dai, T. Kameyama, S. Suzuki and S. Kuwabata, *J. Phys. Chem. C*, 2012, **116**, 21895–21902.
43 L. Tian, H. I. Elim, W. Ji and J. J. Vittal, *Chem. Commun.*, 2006, 4276–4278.
44 Z. Feng, P. Dai, X. Ma and J. Zhan, *Appl. Phys. Lett.*, 2010, **96**, 013104.
45 T. Todorov and D. B. Mitzi, *Eur. J. Inorg. Chem.*, 2010, **2010**, 17–28.
46 M. G. Panthani, V. Akhavan, B. Goodfellow, J. P. Schmidtke, L. Dunn, A. Dodabalapur, P. F. Barbara and B. A. Korgel, *J. Am. Chem. Soc.*, 2008, **130**, 16770–16777.
47 W. Bu, Z. Chen, F. Chen and J. Shi, *J. Phys. Chem. C*, 2009, **113**, 12176–12185.
48 Z. Xu, C. Shen, Y. Hou, H. Gao and S. Sun, *Chem. Mater.*, 2009, **21**, 1778–1780.
49 L. Polavarapu and Q.-H. Xu, *Nanotechnology*, 2009, **20**, 185606.
50 M. Chen, Y.-G. Feng, X. Wang, T.-C. Li, J.-Y. Zhang and D.-J. Qian, *Langmuir*, 2007, **23**, 5296–5304.
51 S. L. Castro, S. G. Bailey, R. P. Raffaelle, K. K. Banger and A. F. Hepp, *Chem. Mater.*, 2003, **15**, 3142–3147.
52 M. Marezio, *Acta Crystallogr.*, 1966, **20**, 723–728.
53 T. Rajasekharan and K. Schubert, *Z. Metallkd.*, 1981, **72**, 275–278.
54 D. Friedrich, O. Kluge, M. Kischel and H. Krautscheid, *Dalton Trans.*, 2013, **42**, 9613–9620.
55 S.-H. Choi, E.-G. Kim and T. Hyeon, *J. Am. Chem. Soc.*, 2006, **128**, 2520–2521.
56 W. Han, L. Yi, N. Zhao, A. Tang, M. Gao and Z. Tang, *J. Am. Chem. Soc.*, 2008, **130**, 13152–13161.
57 S. T. Connor, C.-M. Hsu, B. D. Weil, S. Aloni and Y. Cui, *J. Am. Chem. Soc.*, 2009, **131**, 4962–4966.
58 E. Parthé, K. Yvon and R. H. Deitch, *Acta Crystallogr., Sect. B: Struct. Crystallogr. Cryst. Chem.*, 1969, **25**, 1164–1174.
59 U. Steinbrenner and A. Simon, *Z. Kristallogr.*, 1997, **212**, 428–438.
60 S. Tomić, L. Bernasconi, B. G. Searle and N. M. Harrison, *J. Phys. Chem. C*, 2014, **118**, 14478–14484.
61 D. Friedrich, Ph.D. thesis, Universität Leipzig, 2012.
62 P. Stadelmann, JEMS, Cime-epfl technical report, CIME-EPFL, Lausanne, 2008.